Department of Physics and Astronomy
Heidelberg University

Bachelor Thesis in Physics
submitted by

Hannah Gebhardt

born in Wiesbaden (Germany)

2023

Determination of systematic uncertainties of the J/ψ measurement in ALICE TRD-triggered pp-collisions at $\sqrt{s} = 13$ TeV

This Bachelor Thesis has been carried out by Hannah Gebhardt at the
Physikalisches Institut, Heidelberg University
under the supervision of
Priv. Doz. Dr. Yvonne Pachmayer

Abstract

This thesis focuses on quantifying systematic uncertainties in the extraction of the J/ψ signal from the $J/\psi \rightarrow e^+e^-$ and $J/\psi \rightarrow e^+e^-\gamma$ decay channels. These decays were measured with the ALICE Detector at the LHC in TRD-triggered pp-collisions, with a center-of-mass energy of $\sqrt{s} = 13$ TeV. To assess systematic uncertainties arising from differences in detectors acceptance and efficiency in Data and Monte Carlo (MC), variations in background description, mass cut range, track cuts, and particle identification criteria were employed with respect to the default selection criteria used in the analysis. Additionally, uncertainties stemming from the ITS-TPC matching and the J/ψ kinematics are determined, along with global uncertainties related to luminosity and branching ratio. All uncertainties that do not pass the 'barlow check', and hence are considered systematic, are combined to yield an overall systematic uncertainty of 9.1% over a p_T range from 2 GeV/c to 15 GeV/c. This result serves as a conservative upper estimate of the systematic uncertainties of the J/ψ measurement.

Kurzfassung

Diese Arbeit konzentriert sich auf die Quantifizierung systematischer Unsicherheiten bei der J/ψ-Signalextraktion aus den Zerfallskanälen $J/\psi \rightarrow e^+e^-$ und $J/\psi \rightarrow e^+e^-\gamma$. Diese Zerfälle wurden mit dem ALICE-Detektor am LHC in den Jahren 2017 und 2018 in TRD-getriggerten pp-Kollisionen bei einer Schwerpunktsenergie von $\sqrt{s} = 13$ TeV gemessen. Zur Bewertung der systematischen Unsicherheiten, die aus Abweichungen der Akzeptanz der Detektoren und der Effizienz zwischen gemessenen Daten und Monte Carlo(MC) Simulationen entstehen, werden Variationen in der Hintergrundbeschreibung, im berücksichtigten Massenbereich, bei den auf Spuren angewandten Schnitten und den Kriterien zur Teilchenidentifikation verwendet. Zusätzlich werden Unsicherheiten, die aus dem ITS-TPC-Matching und der J/ψ-Kinematik resultieren, bestimmt. Auch die globalen Unsicherheiten wie die Luminosität und die Verzweigungsverhältnisse werden quantifiziert. Alle Unsicherheiten, die den "Barlow-Test" nicht bestehen und daher als systematisch betrachtet werden, werden kombiniert und ergeben eine gesamte systematische Unsicherheit von 9,1% über einen p_T-Bereich von 2 GeV/c bis 15 GeV/c. Dieses Ergebnis dient als eine konservative obere Schätzung der systematischen Unsicherheiten der J/ψ Messung.

Contents

Chapter 1

Introduction

1.1 Motivation

A Large Ion Collider Experiment (ALICE) is an experiment at the Large Hadron Collider (LHC), dedicated to studying the properties and influence of the quark-gluon plasma (QGP) on particle production. Studying the QGP can provide new insights into the early stage of the universe. ALICE provides the ability to investigate the properties of the QGP by comparing decay measurements from different collision systems, including proton-proton (pp), proton-lead (p-Pb), and lead-lead (Pb-Pb) collisions [12]. An effective method is to compare the production of J/ψ mesons across these various collision scenarios. The $J/\psi \to e^+e^-$ decay channel is well-suited for this due to the good electron identification and triggering capabilities of the Transition Radiation Detector (TRD) to enhance electron/positron samples [13]. In order to obtain reliable results on the J/ψ-production in pp-collisions, it is essential to study and quantify the systematic uncertainties.

1.2 Structure of thesis

The following chapter will give a brief overview over the theoretical background with a special focus on the Standard Model and the J/ψ meson. The experimental setup of ALICE and different detectors are described in chapter 3. After examining the signal extraction procedure, the systematic errors associated with the reconstruction of J/ψ will be analyzed. The results will be interpreted and compared with previous results in chapter 6. Lastly, there will be a summary and an outlook on possible improvements in the future.

Chapter 2

Theoretical Background

2.1 Standard Model of Particle Physics

The Standard Model of Particle Physics (SM) embodies the most accurate and successful theory for describing elementary particles and their interactions. In an attempt to classify the different particles and interactions they are usually grouped based on various characteristics (see Fig. 2.1).

The particles in the SM are classified into fermions (half integer spin) and bosons (full integer spin). For every fermion there is a corresponding anti-matter particle with the same mass but opposite-sign charge. Fermions are the fundamental constituents of matter (or antimatter). They can be further divided into quarks and leptons in three generations. Particles of different generations share the same physical properties except for the mass that increases with higher generation and their mean lifetime. While particles of the first generation are stable and form the basis of the matter that surrounds us, particles of higher generations decay rapidly and, with few exceptions, are only observed in collision experiments.

Gauge Bosons with spin 1 mediate the forces between particles. Photons mediate the electromagnetic force between electrically charged particles. The weak interaction is mediated by W^+-,W^-- and Z^0-bosons between all fermions and has the ability to change the flavour. The weak bosons can also interact with each other through weak interaction. In contrast to photons, W^+-,W^-- and Z^0-bosons are massive. Eight gluons are the force-carriers of the strong force acting between colour-charged particles.

There are six different quark flavours: up (u), down (d), charm (c), strange (s), top (t) and bottom (b). They carry electric charge as well as colour charge. Therefore, quarks participate in strong, electromagnetic and weak interactions. Due to colour-confinement, quarks are confined to bound states with neutral colour charge, that are called hadrons.
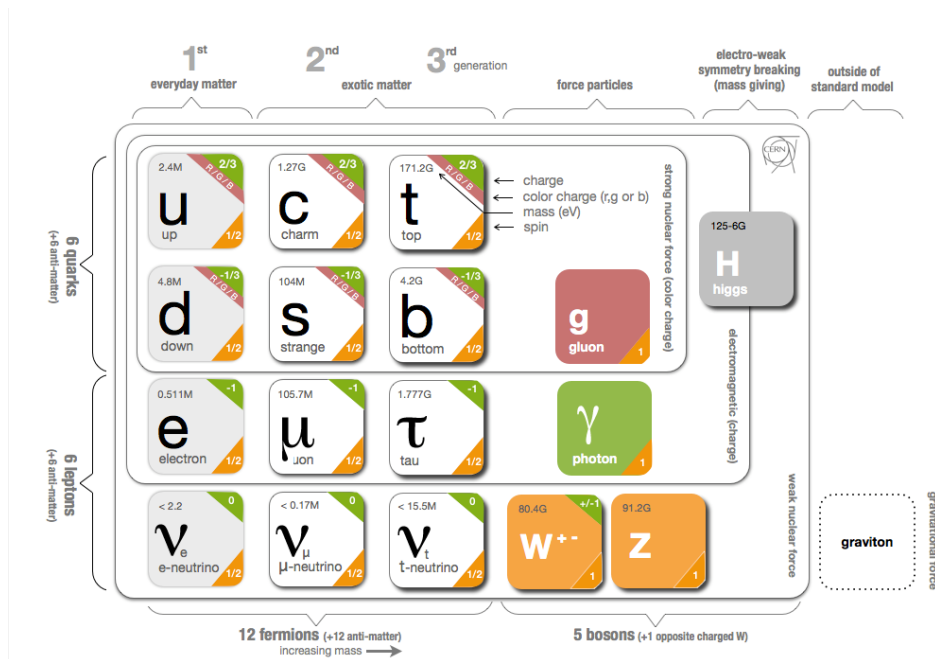
Figure 2.1: Overview of the particles in the Standard Model [19]

These states are dominated by the strong force. Hadrons can either consist of a quark and an anti-quark (meson) or three quarks or antiquarks (baryon). For example, π, K, D and J/ψ are mesons. Protons and neutrons are baryons.

Leptons do not carry colour charge. However some of them interact electromagnetically. The latter are called electron (e^-), muon (μ^-) and tau (τ^-). Neutrinos only interact through the weak force which makes it complicated to study their properties in most experimental setups. The Standard Model predicts them to be massless, however neutrino oscillations requires neutrinos to have a minuscule mass.

For every fermion there is a corresponding anti-matter particle with the same mass but opposite-sign charge.

Although the Standard Model of Particle Physics aligns with most experimental measurements, it does not include gravity and dark matter. Some other effects like neutrino-oscillations also cannot be described by the SM [24].

2.2 Quantum Chromodynamics

The properties of the strong force are described by quantum chromodynamics (QCD). Although quantum electrodynamics (QED) is significantly better understood, QCD theory and experiment align well, enabling reliable statements to be made about the properties and behavior of quarks and gluons.

QCD predicts that quarks only experience an attractive force through gluons if they lead to a colourless bound state (meson or baryon). Otherwise the potential will be repulsive. This results in colour confinement. If the distance between two quarks is increased, their colour-field is squeezed into flux tubes until it is more favourable to create quark-antiquark pairs than to elongate the flux tube. Therefore the force between two quarks is weaker at smaller distances which leads to quarks that act like free particles if they are very close to each other [21].

This Quark-Gluon Plasma (QGP) can be reached at temperatures above $T_C = (156.5 \pm 1.5)$ MeV/k_B [7]. While the QGP can be artificially created and studied in ultrarelativistic heavy-ion collisions at accelerators, it is assumed to have occured in the early universe, approximately $10^{-5} \sim 10^{-4}$ s after the Big Bang. Therefore, experiments that contribute to a better understanding of the QGP can provide new insights into the origin of our universe and its early evolution [29]. The LHC was developed to reach those energies in lead-lead collisions. ALICE provides a unique opportunity to study the characteristics and effects of the resulting QGP on the particle production [11].

2.3 The J/ψ meson

The J/ψ meson consists of a charm and anticharm quark. It has a mass of (3096.900 ± 0.006) MeV/c^2 and a width of (92.6 ± 1.7) keV/c^2 [15].

The discovery of the J/ψ meson can be regarded as a significant milestone in the history of particle physics. It unveiled the presence of the charm quark, thereby confirming the quark model. The magnitude of this revelation is underscored by its name, often referred to as the "November Revolution." On November 10, 1974, two research teams jointly announced the identification of a new particle at an energy of 3095 GeV, with an exceptionally extended lifetime, approximately 1000 times greater than that of particles of similar mass [17]. One of these groups, under the leadership of Burton Richter, conducted their investigation at the Stanford Linear Accelerator Center (SLAC). Richter christened the newly discovered particle "ψ" to align with the convention of naming mesons using Greek letters, and ψ had not been previously assigned. Richter's initial proposal to name the particle "SP" after the SPEAR accelerator at SLAC was met with disapproval by his colleagues. Interestingly, later spark chamber images often resembled the ψ shape [20].

Samuel Ting led the research team based at the Brookhaven National Laboratory (BNL). He designated the particle as "J." This choice emerged because "J" is the subsequent letter after K, which was the name assigned to the previously identified strange meson. It's worth noting that the Latin letter "J" bears a resemblance to the Chinese character for Ting's surname. Despite this coincidence, Ting firmly maintained that it did not

$J/\psi(1S)$ DECAY MODES

	Mode		Fraction (Γ_i/Γ)	Scale factor/ Confidence level
Γ_1	hadrons		(87.7 $\pm$ 0.5) %	
Γ_2	virtual $\gamma \to$ hadrons		(13.50 $\pm$ 0.30) %	
Γ_3	ggg		(64.1 $\pm$ 1.0) %	
Γ_4	$\gamma g g$		(8.8 $\pm$ 1.1) %	
Γ_5	$e^+ e^-$		(5.971 $\pm$ 0.032) %	
Γ_6	$e^+ e^- \gamma$	[a]	(8.8 $\pm$ 1.4) $\times 10^{-3}$	
Γ_7	$\mu^+ \mu^-$		(5.961 $\pm$ 0.033) %	

Figure 2.2: Decay channels of the J/ψ-meson [15]

influence his selection of the name.[25]

In recognition of their groundbreaking work, Richter and Ting were jointly honored with the 1976 Nobel Prize in Physics [25].

Like most mesons, the J/ψ particle decays shortly after its formation into various decay products. To investigate the production of J/ψ, it is necessary to calculate the invariant mass of reconstructed particles that could have originated from a J/ψ decay. As shown in Fig. 2.2 most J/ψ mesons decay into hadrons. Examining these decays leads to a high background which results in large uncertainties in the signal extraction. Therefore, oftentimes the decay $J/\psi \to e^+e^-$ and the radiative decay $J/\psi \to e^+e^-\gamma$ are more suitable to study the J/ψ with high precision.

In this thesis, particular attention is given to the J/ψ meson due to its sensitivity to changes in the presence of a Quark-Gluon Plasma (QGP) formed during heavy-ion collisions. At lower energies, a few c and $\bar{c}$ quarks are produced in the collision process. In high-energy heavy ion collisions, more c and $\bar{c}$ quarks are created. Subsequently, the QGP forms, leading to the separation of these quark-antiquark pairs. As the system cools down, a process called hadronization takes place, resulting in the combination of these heavy quarks with lighter quarks. This combination leads to the production of D-mesons (c or $\bar{c}$ with $u/\bar{u}$, $d/\bar{d}$, or $s/\bar{s}$) and J/ψ mesons.

The higher number of c and $\bar{c}$ quarks increases the likelihood of producing J/ψ mesons during the hadronization stage [8]. By comparing the number of J/ψ in proton-proton and heavy-ion collisions, it becomes possible to study the properties of the QGP and particle production at different energy levels.

Additionally, other predictions from the theoretical foundations of QCD, such as QCD perturbation theory, can be explored in pp-collisions [23]. While the production of $c\bar{c}$ pairs is perturbative, the formation of J/ψ cannot be adequately described using this approach alone, as it needs an additional gluon. Given the complexity of this process in theoretical terms, comparing various theoretical descriptions with experimental data

allows for further research aimed at improving the underlying theory.

2.4 Particle Detection

To accurately detect particles generated during a collision, it is essential to comprehend their interaction with the detector material. When a charged, relativistic particle traverses the detector material, it undergoes energy loss through the ionization of atoms. This distinctive energy loss can be used for particle identification and is mathematically expounded by the Bethe-Bloch equation [24]:

$$-\left\langle \frac{\mathrm{d}E}{\mathrm{d}x} \right\rangle \approx n_e 4\pi r_e^2 m_e c^2 z^2 \frac{1}{\beta^2} \left\{ \ln \left[\frac{2\beta^2 \gamma^2 c^2 m_e}{I_e} \right] - \beta^2 \right\} \tag{2.1}$$

n_e electron density $n_e = \rho N_a \frac{Z}{A}$

r_e classical electron radius $r_e = \frac{e}{4\pi m_e c^2}$

m_e electron mass

c speed of light

z charge number

β $\beta = \frac{v}{c}$

γ $\gamma = \frac{1}{\sqrt{1-\beta^2}}$

I_e effective ionisation potential

The noteworthy characteristic of the Bethe-Bloch equation is that particles sharing the same $\beta\gamma$ value but with distinct masses, will exhibit different patterns of energy loss within the detector when considered as a distribution of momentum.

In Figure 2.3, the Bethe-Bloch equation is plotted as a function of momentum. The three distinct regions of the Bethe-Bloch equation are easily identifiable. At low $\beta\gamma$ values, particles exhibit reduced velocities, which allows them to release energy within the detector material since they spend longer times within the material. The energy deposition per unit length diminishes proportionally to $1/\beta^2$ for elevated momentum, reaching a minimum around $\beta\gamma \approx 3 - 4$. Particles with a momentum in this interval are denoted as 'minimum ionizing particles'. As $\beta\gamma$ increases beyond this range, the energy deposition becomes logarithmically proportional to $\ln \beta^2\gamma^2$, which is commonly referred to as the relativistic rise. Here, the polarization, which depends on density, begins to affect the energy deposition. As the transverse electric field increases due to Lorentz transformation, the medium's polarization effectively shields the electric field at greater distances, reducing the long-range contribution and resulting in a plateau.

Additionally, Figure 2.3 illustrates how various particles leave distinct traces in the momentum-dependent energy deposition distribution. These differences arise from their
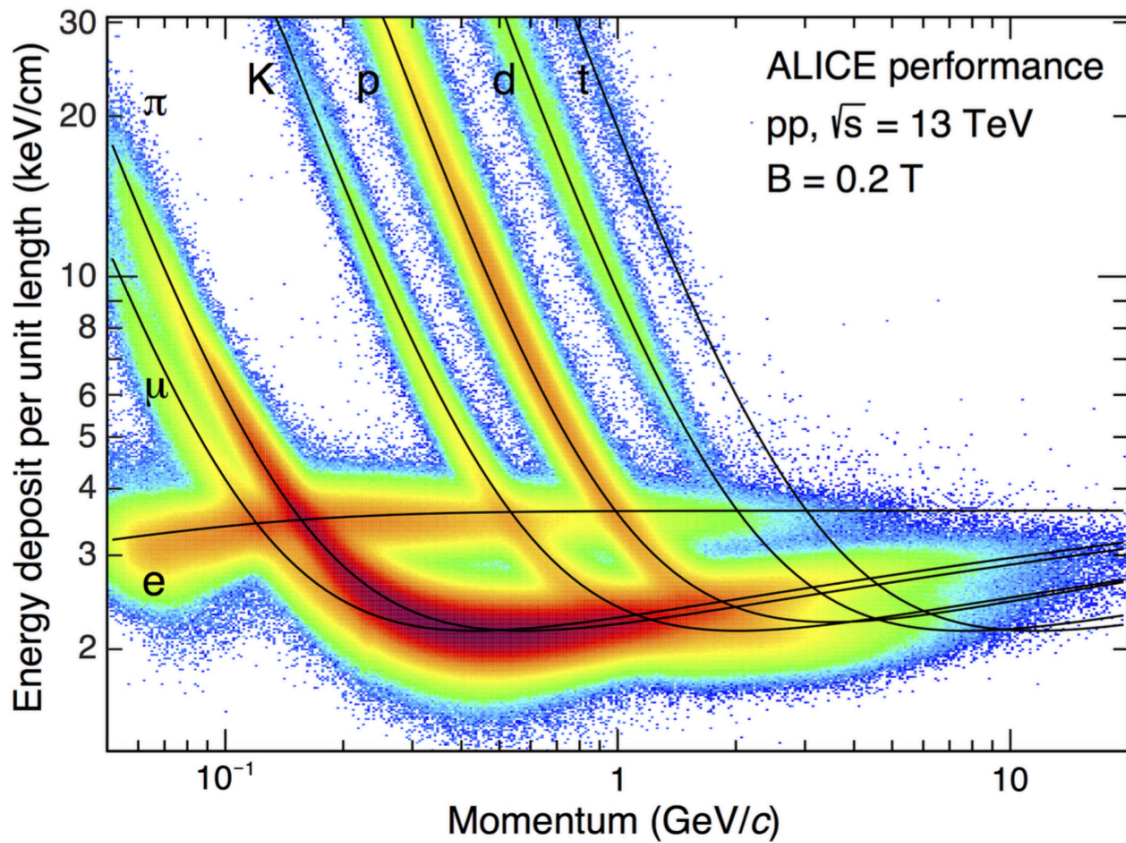
Figure 2.3: Energy loss in TPC used for particle detection [10]

varying masses. The energy deposition per unit length for electrons appears significantly different from that of other particles because electrons are already in the relativistic rise region within the covered momentum range of the plot. Heavier particles are depicted further to the right in their traces.

Chapter 3

Experimental Setup

3.1　A Large Ion Collider Experiment (ALICE)

Situated at the Large Hadron Collider (LHC), the ALICE detector plays a central role in the research efforts of the European Organization for Nuclear Research (CERN). It is one of the key experiments conducted at the LHC along with LHCb, ATLAS, and CMS. ALICE takes on a pioneering role by focusing on studying heavy-ion collisions. These collisions create incredibly high energy densities and high temperatures, providing an exceptional opportunity to closely examine properties related to the Quark-Gluon Plasma (QGP). While weighing approximately 10000 tons and having dimensions of 16m x 16m x 26m, the ALICE detector enables the detection of particles produced in proton-proton collisions at the LHC. During Run 2, the data-taking period utilized in this analysis, protons collided with a center-of-mass energy of $\sqrt{s} = 13$ TeV [12].

The experiment employs an array of detectors arranged cylindrically around the collision point (refer to Fig. 3.1). Each detector specializes in measuring specific properties of the resulting particles. By pooling the data from these diverse detectors, it is possible to recreate the paths, momentum, and charges of the particles involved. This reconstruction process aids in modeling parent particles based on their decay products, contributing to a deeper understanding of the particles generated in the collision process [12]. While all detectors are vital for the experiments, this thesis will emphasize the three most critical ones for measuring J/ψ decays: the ITS (Inner Tracking System), the TPC (Time-Projection Chamber) and the TRD (Transition Radiation Detector). Their positions within ALICE are illustrated in Fig.3.1.
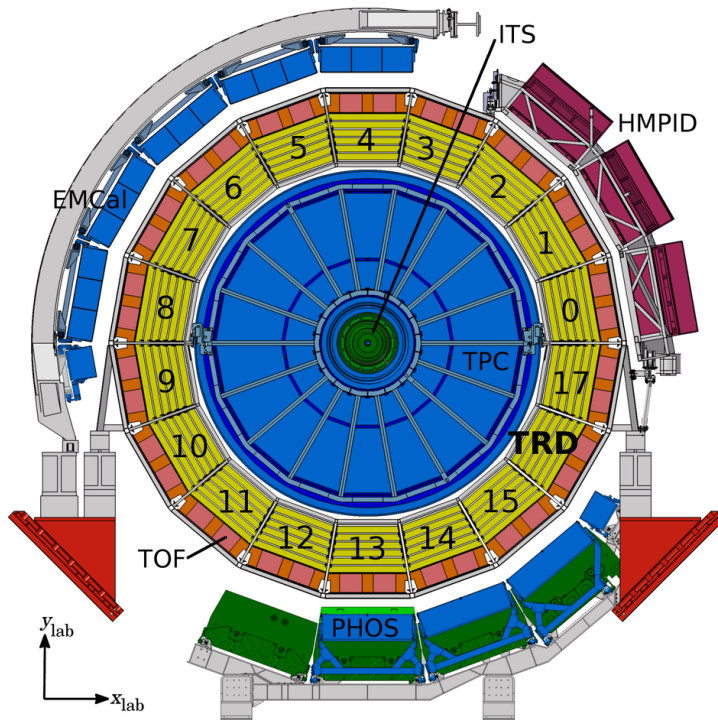
Figure 3.1: Cross section of ALICE with central barrel detectors [13]

3.2   Inner Tracking System (ITS)

Depicted in Fig. 3.1, the ITS constitutes the innermost layers of detectors within ALICE. Consisting of six layers of silicon-based detectors, the ITS covers a pseudorapidity range of $|\eta| < 0.9$. Its principal function involves the high-resolution determination of the primary vertex, secondary vertex reconstruction, particle track measurement, and particle identification (PI), particularly within the lower momentum spectrum (< 200MeV/c). Moreover, it contributes to enhancing the precision of particles reconstructed by the TPC, as well as measuring momentum and reducing background. The configuration is segmented into three parts. The two innermost layers are the Silicon Pixel Detectors (SPD), which are well-suited to handle the increased particle density near the collision point. Subsequently, the two layers are made from Silicon Drift Detectors (SDD) and two layers of double-sided Silicon micro-Strip Detectors (SSD).[12].

3.3   Time Projection Chamber (TPC)

The TPC surrounds the ITS, serving as a critical component. Its primary function encompasses the high-resolution measurement of charged-particle momentum and effective discrimination between two concurrent tracks. Additionally, it fulfills roles in particle identification and vertex determination. Encompassing a pseudorapidity range of $|\eta| < 0.9$, the TPC spans an elevated p_T interval of $(0.1 - 100)$ GeV/c with exceptional momentum resolution. Structurally, the cylindrical detector features an inner radius of 85 cm, an outer

radius of 250 cm, and extends to a length of 500 cm. Its interior is filled with a mixture of $Ne/CO_2/N_2$ (90/10/5) [12]. When a charged particle traverses the detector, the gas is ionized along its path. Due to the applied electric field, the ionization electrons drift towards the segmented end plates. By also measuring the time required for this process, the three-dimensional trajectory of the charged particle can be accurately reconstructed within the detector. The trajectory as well as the magnetic field with $B = 0.5$ T are used in order to detect the momentum of the produced particles [4].

3.4 Transition Radiation Detector (TRD)

The TRD operates on the principle of transition radiation (TR), which arises when a charged particle traverses the interface between two materials with differing dielectric constants. This action generates a mirror charge within the second material as the particle approaches, resulting in a dynamic dipole configuration that emits photons [14]. Within the TRD, electrons exhibit high relativistic behavior ($\gamma \gtrsim 800$), thus emitting radiation in the X-ray spectrum. To effectively detect this phenomenon, multiple material interfaces are essential, given that the production of TR photons per boundary crossing is proportional to the fine structure constant ($\alpha \approx 1/137$).

18 sectors, each containing 30 read-out chambers arranged in 6 layers and 5 stacks form the TRD detector. In order to minimise the material before the Photon Spectrometer (PHOS), in sectors 13-15 the chambers of the middle-stack were not installed. The detector covers a pseudorapidity of $-0.84 < \eta < +0.84$ and the full azimuthal angle.

Each detection chamber is compartmentalized into three principal sections: the radiator, the drift region, and the amplification region. The radiator material is constructed from fiber/foam composites, while the drift and amplification region is filled with a $Xe - CO_2(85 - 15)$ gas mixture [13].

Two main purposes of the TRD are identifying particles and reconstructing their paths. To identify particles, the TRD measures how much energy they lose and if they emit transition radiation. The main aim is to tell apart hadrons, especially pions, while efficiently detecting electrons. The TRD can reject around 99% of pions while being 90% efficient at finding electrons. This makes it crucial for reducing hadronic background in measurements of electrons [13].

3.5 Data Sample

The data sample analyzed in this thesis was gathered during the proton-proton collision run at $\sqrt{s} = 13$ TeV in the years 2017 and 2018. This data can be split into distinct data

variable	trigger condition
p_T	$2 \frac{\text{GeV}}{\text{c}} \left(2\frac{GeV}{c}\right)$
PID value	130 (165)
Minimum TRD tracklets/track	5 (5)
Sagitta cut	$0.2\frac{\text{GeV}}{\text{c}}$ (not applied)
Hit in first layer	required (applied)

Table 3.1: TRD trigger conditions (MC simulation conditions in parenthesis)[27]

collection periods, where no modifications occur in either the beam or the detector setup. Each period consists of multiple runs, encompassing data collection until either the beam ceases or a detector malfunction occurs. During the data collection procedure, the single electron TRD-trigger applies cuts online with a p_T threshold of 2 GeV/c, in addition to a PID threshold in order to select only events with a minimum of one electron [13]. The TRD trigger conditions can be found in table 3.1.

With this trigger, $6.74703 \cdot 10^7$ events were recorded in 2017, and $1.06058 \cdot 10^8$ events in 2018. The visible cross section is determined via van der Meer scans. The results from [9]: $\sigma_{vdM_{2017}} = (58.10 \pm 0.04)$ mb and $\sigma_{vdM_{2018}} = (57.52 \pm 0.03)$ mb lead to a total luminosity of 1.712e+09 mb^{-1} for both years, taking into account the trigger enhancement factor 569.679, which is the ratio between minimum bias events and minimum bias events that satisfy the TRD-trigger conditions [18].

3.6   Monte Carlo Simulations

To quantify the efficiency of the applied selection criteria and understand the reconstructed J/ψ signal distribution, Monte Carlo (MC) simulations are used. For the simulation, the PYTHIA program [22] is employed to simulate the collision, considering its kinematic characteristics. The detector's performance during each specific run is reflected in the simulation. In an effort to manage data efficiently, a J/ψ particle is introduced into each simulated event since the primary interest centers around events featuring at least one J/ψ. Among these introduced J/ψ particles, 70% are designated as prompt J/ψ, adhering to a realistic p_T-spectrum for $p_T > 0$ GeV/c. For $p_T > 6$ GeV/c, a flat spectrum, though not an accurate representation of reality, is employed to enhance statistics in the high transverse momentum range. The remaining 30% of the introduced particles are non-prompt J/ψ particles originating from B-meson decays.

To simulate the J/ψ decay into $e^+ + e^-$ or $e^+ + e^- + \gamma$, the PHOTOS program [28] is used. Subsequently, the particle tracks as they traverse the detector material are simulated using GEANT3 [16] and the standard ALICE reconstruction is run. This process generates a dataset closely resembling the structure of the measurement data but enriched with MC truth information, thereby allowing comparative analysis and validation.

Chapter 4

Signal extraction

The aim of this data analysis is to identify the J/ψ candidates from among all the triggered events that encompass both, a positron and an electron. To achieve a distinct signal, cuts are applied to reduce background originating from other particles undergoing decays into e^+e^-, misidentified hadrons or e^+e^- pairs that don't originate from the same particle. The efficiency of these cuts, acquired through Monte Carlo simulations, can be utilized to correct the measurements, enabling the determination of the J/ψ yield from the raw signal.

4.1 Track selection

The criteria in Table 4.1 are applied, to select tracks that are optimally suited for the analysis.

variable	cut value
require ITS refit	yes
require TPC refit	yes
$N^{\mathrm{TPC}}_{\mathrm{clusters}}$	$70 < N^{\mathrm{TPC}}_{\mathrm{clusters}} < 159$
χ^2_{TPC}percluster	$0 < \chi^2_{TPC} < 4$
reject kinks	yes
$|\eta|$	$-0.84 < \eta < 0.84$
p_{T}	$1.0\ \mathrm{GeV/c} < p_{\mathrm{T}} < 100\ \mathrm{GeV/c}$
require SPD any	yes
χ^2_{ITS}percluster	$0 < \chi^2_{ITS} < 36$
$|\mathrm{DCA_{xy}}|$	$< 1.0\mathrm{cm}$
$|\mathrm{DCA_z}|$	$< 3.0\mathrm{cm}$

Table 4.1: Single-track selection criteria used in the reconstruction of J/ψ signal distribution

Both the ITS and TPC refit conditions are essential to guarantee accurate track reconstruction and precise particle identification. The TPC demands a cluster count ranging from 70 to 159, as the overall cluster count stands at 159. Enforcing a minimum of 70 clusters in the TPC ensures an ample signal for reliable path reconstruction and PID. Further ensuring good track reconstruction involves constraining χ^2_{TPC} to be less than 4.

If a reconstructed track exhibits a kink, there is a high probability that it originated from a charged mother particle undergoing a decay, which is irrelevant to the analysis of J/ψ mesons. As these decay processes are not pertinent to the J/ψ analysis, tracks displaying kinks are discarded.

The pseudorapidity η cut arises from the detector coverage considerations. Specifically, the ITS and TPC encompass a region of $|\eta| < 0.9$, whereas the TRD coverage is confined to $|\eta| < 0.84$. Consequently, data obtained within this defined range are used for the analysis, as they contain information from all crucial detectors.

A minimum transverse momentum cut is set at 1GeV/c. Primarily, this decision arises from the fact that electrons below this momentum range exhibit an energy loss that considerably overlaps with the energy loss of other particles. Consequently, these lead to an elevated background level.

To minimize the impact of secondary particles, which may arise from interactions between particles and the detector material within the ITS, the selection criterion SPDany is implemented. This criterion guarantees the presence of at least one signal in the SPD, the two innermost layers of the ITS. Furthermore, the χ^2_{ITS} parameter, which serves as an indicator of track reconstruction quality within the ITS, is constrained to exclude bad reconstructions.

The distance of closest approach (DCA), denoting the minimum separation between a particle's reconstructed trajectory and the primary vertex in the x-y or z plane, undergoes constraints both in the x-y and z direction. These criteria serve to eliminate particles originating from weak particle decays and interactions with detector material, thereby refining the analysis results.

4.2 Particle Identification

While certain track selection criteria have an impact on particle identification, additional cuts are implemented to guarantee that electrons are identified with high precision since they are used to reconstruct the J/ψ signal.

variable	cut value for $p_T < 5 \text{GeV}/c$	cut value for $p_T > 5 \text{GeV}/c$
n_{σ_e}	$\in [-3.0, 3.0]$	$\in [-3.0, 3.0]$
n_{σ_p}	>3.0	>2.0
n_{σ_π}	>3.0	>2.0

Table 4.2: Particle identification criteria used in the reconstruction of J/ψ signal distribution

The particle identification threshold of the TPC is defined within the interval [-3.0, 3.0] for electrons. The rejection criteria for protons and pions vary according to momentum, a measure taken to increase the efficiency at high momenta.

4.3   Background estimation

During the e^+ and e^- pairing process, the majority of pairs do not originate from J/ψ decays and are hence classified as background. When paired leptons lack a shared mother particle and consequently do not have a common physical origin, they are regarded as uncorrelated background. On the other hand, correlated background arises from hadronic decays or jet fragmentations. To accurately characterize this background, the hybrid signal extraction method is employed.
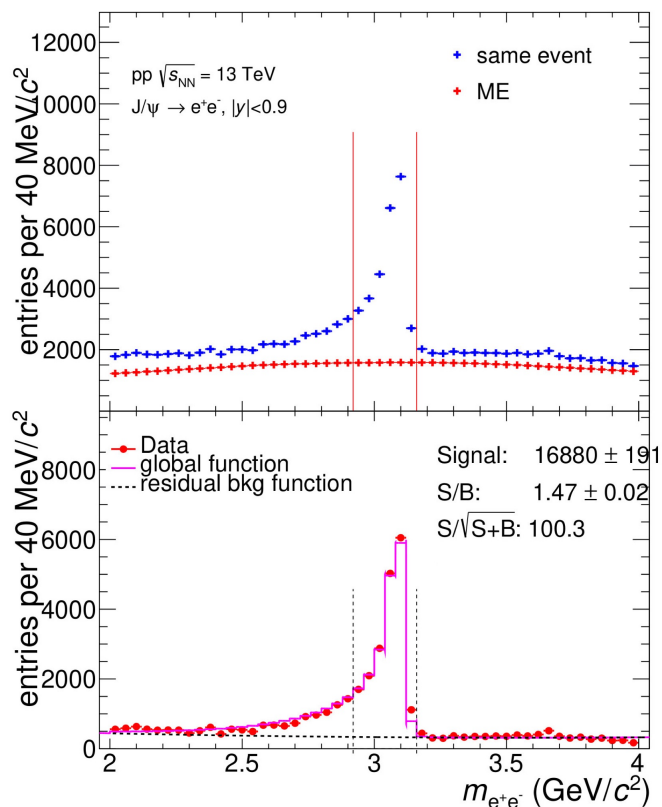

Figure 4.1: Signal extraction with background estimation for $p_T = (3.0 - 3.25)$ GeV/c; mass cut range marked by vertical lines

The uncorrelated background is determined using unlike-sign (US) pairs extracted from mixed events (ME). As the dataset used for this pairing is significantly higher than the one employed for signal extraction, the results are rescaled to the e^+e^--distribution, with the peak from the J/ψ signal being excluded. To achieve this scaling, the like-sign (LS) pair distribution within the same event (SE) is utilized to calculate the ratio $(SE - LS)/(ME - LS)$. The ME and same event distribution is displayed in Figure 4.1 in the upper plot. It is well visible that the ME signal roughly follows the shape of the same event distribution in the regions that are not dominated by the J/ψ signal.

Conversely, the remaining background that represents the correlated background, is characterized through a fit function. To describe the J/ψ signal, the MC signal shape is used. The empirical fit function follows a second-order polynomial. In Figure 4.1 the lower plot depicts the measured data as well as the fit function and the resulting global function. Here it is visible that the global fit function represents the data in the region where it is mostly dominated by background as well as in the region of the J/ψ-signal.

4.4   Mass cut range

The invariant mass of the two matched leptons should correspond to the invariant mass of the mother particle. Therefore, the mass distribution is employed to quantify the number of J/ψ particles that were detected. To accomplish this, mass cuts need to be defined. These cuts specify the range within which the e^+ and e^- are considered to originate from a J/ψ decay. For the default analysis, this mass range is set to $[2.92 - 3.16]$ GeV/c^2. In Figure 4.1, the mass cut range is marked by red (top) and dotted (bottom) vertical lines.

4.5   p$_T$-binning

In previous analyzes, the binning of transverse momentum p$_T$ was notably wide, due to limited statistics. However, with the TRD-triggered data obtained during run 2, it has become possible to establish a finer-grained binning strategy, all while maintaining favorable Signal/Background (S/B) ratios and high statistical precision across all bins. "Background" refers to the correlated and the uncorrelated background meaning all e^+e^--pairs that do not originate from the same J/ψ-decay. The not-efficiency corrected p$_T$-differential J/ψ distribution, corrected for binwidths, as well as the S/B ratio, are depicted in Fig. 4.2.

Clearly, the distribution of the binwidth-corrected J/ψ signal conforms to the anticipated shape, as expounded in [1]. Starting the p$_T$ distribution at 2 GeV/c is a result of the TRD trigger's condition, which requires p$_T > 2$ GeV/c for just one of the electrons. Con-
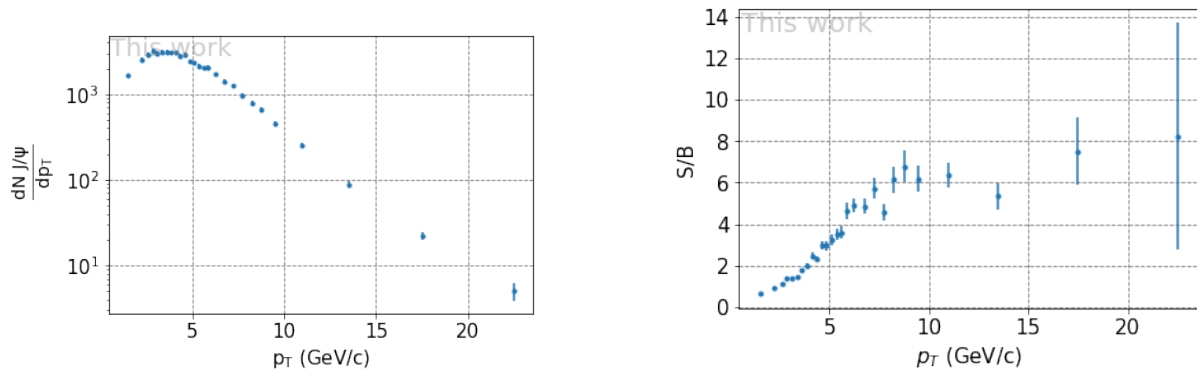
Figure 4.2: p_T-binwidth corrected p_T-differential J/ψ-distribution with statistical uncertainties (left) and S/B-ratio vs p_T with statistical uncertainties (right)

sequently, the second electron could result in a p_T value lower than two. The maximum p_T value observed is 40 GeV/c. For higher p_T values, the statistics are insufficient for data extraction.

The S/B ratio exhibits its lowest values for small p_T values. In the p_T-bin $(2.0 - 2.5)$ GeV/c, the S/B ratio is 0.93 ± 0.05. Though it increases with higher transverse momenta, it remains rather constant from the p_T-bin $(8.0-8.5)$ GeV/c with $(S/B) = 6.1\pm0.6$ to the p_T-bin $(15.0 - 20.0)$ GeV/c with $(S/B) = 7.5 \pm 1.6$.

The resulting significance, defined as $\frac{S}{\sqrt{S+B}} = \frac{S}{\sigma_S}$, is presented in Figure 4.3. Figures illustrating the relative uncertainties and the χ^2_{red} for the background fit vs p_T can be found in Fig. 4.4.

The relative uncertainties are calculated by taking the ratio of the total uncertainty and the signal. They remain consistently at 5% across the entire p_T range up to 13 GeV. Consequently, the adoption of a finer binning for small transverse momenta is highly appropriate for the analysis, as high statistics support this choice. For the region beyond 13 GeV, however, a larger binning becomes essential to ensure trustworthy results due to the limitations in statistics.
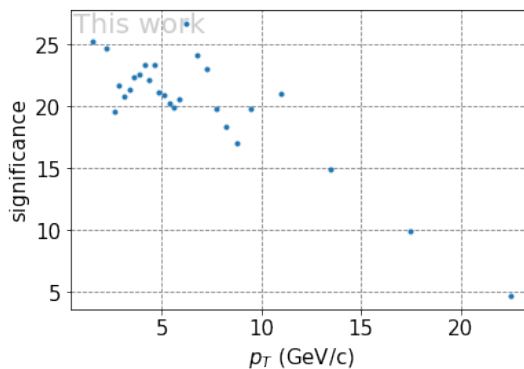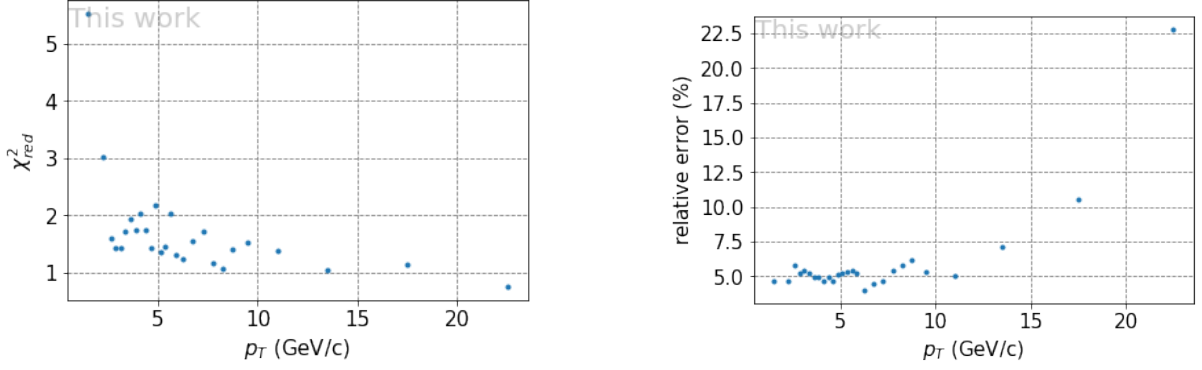

Figure 4.3: significance vs p_T

Figure 4.4: χ^2 (left) and relative uncertainties (right) as a function of p_T

With the χ^2_{red} serving as a measure of how well the fit represents the measured data, and $\chi^2_{red} = 1$ indicating an optimal fit, it is evident that the fit used for background description performs best in the higher p_T range. Nevertheless, even the χ^2_{red} values in the lower transverse momentum bins remain acceptable. The only exception is the value in the first bin with a range of $(0.0 - 1.0)$ GeV/c, which has a significantly higher value of $\chi^2_{red} = 5.2$ compared to the other bins. This discrepancy might lead to less reliable results in this particular bin.

24

Chapter 5

Analysis of systematic uncertainties

5.1   Systematic uncertainties

First of all, the term "systematic uncertainty" has to be defined. Roger Barlow provides a definition of systematic uncertainties, stating that "Any uncertainty in the process whereby your raw data is converted into a published result is a systematic error" [5]. It is crucial to differentiate between systematic uncertainties and systematic errors. A systematic error might involve using the incorrect settings on a multimeter or encountering a broken cable in the experimental setup. Unlike random errors, systematic uncertainties do not arise from the statistical characteristics of the underlying process. If the systematic uncertainty is known in advance, it can be viewed as a bias that can be rectified during the data collection phase. This also implies that an unknown bias constitutes a systematic uncertainty [6].

5.2   Barlow check

There is no single approach to determine systematic uncertainties for complex experiments and data analyzes that yield an overall satisfactory result. In this thesis, e.g. variations of the applied selection criteria, or methods to determine the background, are employed to provide a preliminary and rather conservative estimation of the systematic uncertainties. When employing this method, it is crucial to evaluate whether the difference between two sets of cuts is statistically significant. This assessment helps to determine whether the observed discrepancy can be considered a systematic uncertainty.

If two different sets of cuts are utilized in the analysis, one might obtain the result $a_1 \pm \sigma_1$ with the default setting and $a_2 \pm \sigma_2$ with a variation. The difference between these results,

denoted as $\Delta = a_1 - a_2$, is associated with an error of:

$$\sigma_\Delta^2 = \sigma_1^2 + \sigma_2^2 - 2\rho\sigma_1\sigma_2 \tag{5.1}$$

with an unknown correlation ρ. It is possible to establish constraints on ρ by using a weighted average and the Minimum Variance Bound. Knowing limits to ρ translates into limitations on σ_Δ (for a more detailed derivation refer to [6]).

These limitations can serve as a means to assess the disparity between the results obtained from two different sets of cuts. It is customary to conclude that a difference of less than 1σ suggests that the test is successfully passed, attributing the variation solely to statistical fluctuations. If the discrepancy exceeds 4σ, the assessment is unsuccessful. Hence, depending on how conservative the estimation of systematic uncertainties should be, the limiting value for the decision upon whether the test is passed is set between 1σ and 4σ. For this analysis, a test is considered failed if it exceeds a threshold of 2σ. In such cases, the next step involves investigating whether any errors occurred during the analysis that may have contributed to the substantial deviation. Following a thorough examination of all potential sources of error and consistently obtaining the same results, the disparity can then be deemed a systematic uncertainty.

5.3 Determination of systematic uncertainties

Variations in the background description, the mass cut, different track- and PID-cuts are examined. The signal, meaning the number of J/ψ after subtracting the background and counting within the mass range, obtained through the variation method is divided by the corresponding efficiency. Subsequently, this result is divided by the ratio of the signal obtained with the default cuts described in Chapter 4 to its corresponding efficiency. The efficiencies are determined using MC simulations and ideally should result in a scenario where the description of the real measurement converges to the same outcome regardless of the variation. Consequently, systematic uncertainties can arise from inaccuracies in the MC simulations. To evaluate whether the deviation from a value of 1 arises due to systematic uncertainties, the Barlow error is calculated as follows:

$$\text{barlowerror} = \sqrt{\left|\left(\frac{\Delta_\text{default}}{\text{default}}\right)^2 - \left(\frac{\Delta_\text{variation}}{\text{variation}}\right)^2\right|} \tag{5.2}$$

"Default" refers to the number of J/ψ particles obtained using the default cuts described in Chapter 4, with Δ_default representing the uncertainty associated with this result. Accordingly, "variation" denotes the signal obtained with the altered cuts, and $\Delta_\text{variation}$

represents the corresponding uncertainty.

The barlow-error can then be used to calculate the barlow-value.

$$\text{barlowvalue} = \left| \frac{\text{default} - \text{variation}}{\text{barlowerror}} \right| \Rightarrow \begin{cases} \text{passes} & < 2\sigma \\ \text{fails} & > 2\sigma \end{cases} \tag{5.3}$$

If a variation does not pass the Barlow check, it will be included in the systematic uncertainties of the J/ψ measurement.

Other uncertainties related to the ITS-TPS matching, J/ψ kinematics in MC, luminosity, and branching ratio require different methods to determine their magnitude. These will also be explained in this chapter.

5.3.1 Background description

As described in Section 4.3, the background of the signal can be estimated by employing a combination of mixed event distribution for the uncorrelated background, along with a fit function and a Monte Carlo model for the correlated background and the J/ψ signal. However, it is important to note that using a fit function to describe the correlated background is mostly empirical. Hence, it is essential to compare the results of this background estimation with results obtained using different fit functions or methods to describe the background.

The following methods were compared to the default setting of ME combined with a second-order polynomial fit, scaled to the SELS distribution:

Like-sign (LS) arithmetic and LS geometric methods utilize the count of pairs of like-signed leptons (e^-e^- or e^+e^+) as an estimate of the background. These pairs cannot originate from the same J/ψ. This background estimation heavily relies on statistics, making it a suitable description for the background at low p_T where the number of like-sign pairs is large. However, at higher p_T, statistics are limited, suggesting that alternative background estimation methods may perform better within that range. The first method employs an arithmetic mean, while the second method employs a geometric mean for the amount of LS pairs in each mass-bin. An arithmetic mean is employed for independent events, whereas the geometric mean is typically more appropriate for datasets that display correlation among their values. Another significant property is that the arithmetic mean is sensitive to outliers, reacting strongly to them, while the geometric mean is less affected by outliers, responding more moderately.

Using either a second-order polynomial or a combination of an exponential function with a second-order polynomial provides a background description that remains independent

of the statistics. For this method, the signal is described using the MC signal shape while the remaining background is described by fitting a function to the measured data. This approach should yield consistent results across the entire p_T range. However, when relying solely on a fit function, the uncorrelated background might be inadequately characterized, potentially resulting in discrepancies between the measured and fitted background.

The ME method primarily serves to model the uncorrelated background. Consequently, relying solely on ME neglects the correlated background, potentially resulting in an incomplete background description. To address this issue, ME can be complemented with a fit function. Since this fit function is empirical, various alternatives are used as variations. Additionally, different variations take into account the choice between using the SELS or the SEOS distribution for rescaling the ME invariant mass distribution.

- LS arithmetic

- LS geometric

- Background fit second order polynomial

- Background fit exponential function + second order polynomial

- ME and second order polynomial SELS

- ME and exponential function SELS

- ME and second order polynomial SEOS

- ME and exponential function SEOS

- ME and zero polynomial SEOS

Figure 5.1 depicts the χ^2_{red} distribution of various background description methods. As anticipated, in the lower p_T range, the LS methods provide a superior background description
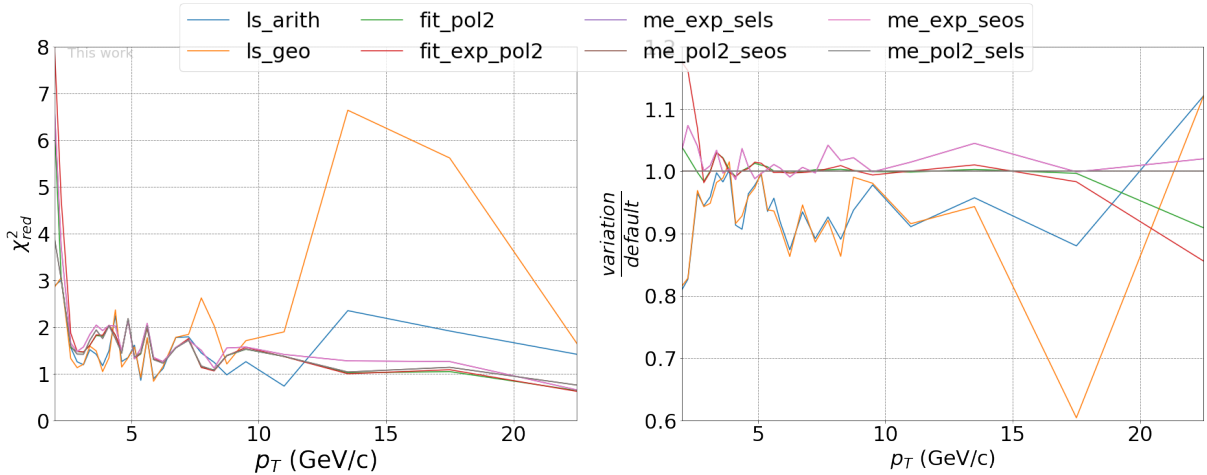

Figure 5.1: χ^2_{red} and variation of different background description methods
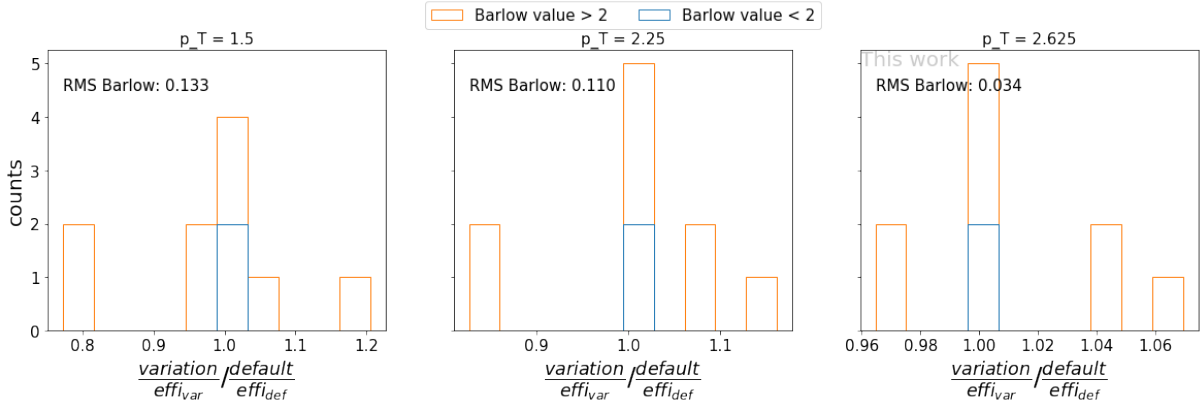
28

Figure 5.2: Variation of different background description methods for individual p_T-intervals between 1 GeV/c and 3 GeV/c

compared to the other methods, while exhibiting higher deviations at $p_T > 12.5$ GeV/c. On the other hand, methods employing only a fit function or a combination of a fit function and ME appear to be quite similar in their performance. Their respective χ^2_{red} values indicate that their background description is less accurate in the lower p_T range but offers a satisfactory description throughout the higher p_T.

The $\frac{variation}{default}$ distribution reveals a distinction between the LS and other methods. Specifically, the LS methods yield fewer counts of J/ψ, whereas all other methods produce higher counts of J/ψ. When comparing the LS data with the results of other methods, it should be noted that the LS method leads to a higher statistical uncertainty.

In the next step, the Barlow check is implemented. Subsequently, histograms are generated for the variations in different p_T bins (see Figure 5.2 for three bins and A.1 for all bins). Variations that pass the Barlow check are excluded from further analysis. Next, assuming this distribution follows a Gaussian distribution, the combination of the standard deviation (σ_{rms}) and the deviation of the mean (μ) from 1 can be considered as the resulting uncertainty:

$$\text{uncertainty} = \sqrt{\sigma^2_{rms} + (\mu - 1)^2} \tag{5.4}$$

These resulting uncertainties do not vary significantly across the range of 2.5 GeV/c < p_T < 15 GeV/c. Calculating the mean of the uncertainties in all p_T-bins in this interval yields an uncertainty of 3.19%. For $p_T < 2.5$ GeV/c, the uncertainty amounts to 12.34%, and for $p_T > 15$ GeV/c, the uncertainty is 11.63%. The high errors could be a result of low statistics in the high p_T-bins. This can be checked by using a wider binning with one bin from $[12 - 20]$ GeV/c and one bin from $[20 - 40]$ GeV/c. Repeating the analysis with this binning leads to variations that pass the barlow check and are therefore considered statistical fluctuations. Hence, the statistical uncertainties dominate in this region which makes measurements at $p_T > 15$ GeV/c unreasonable.
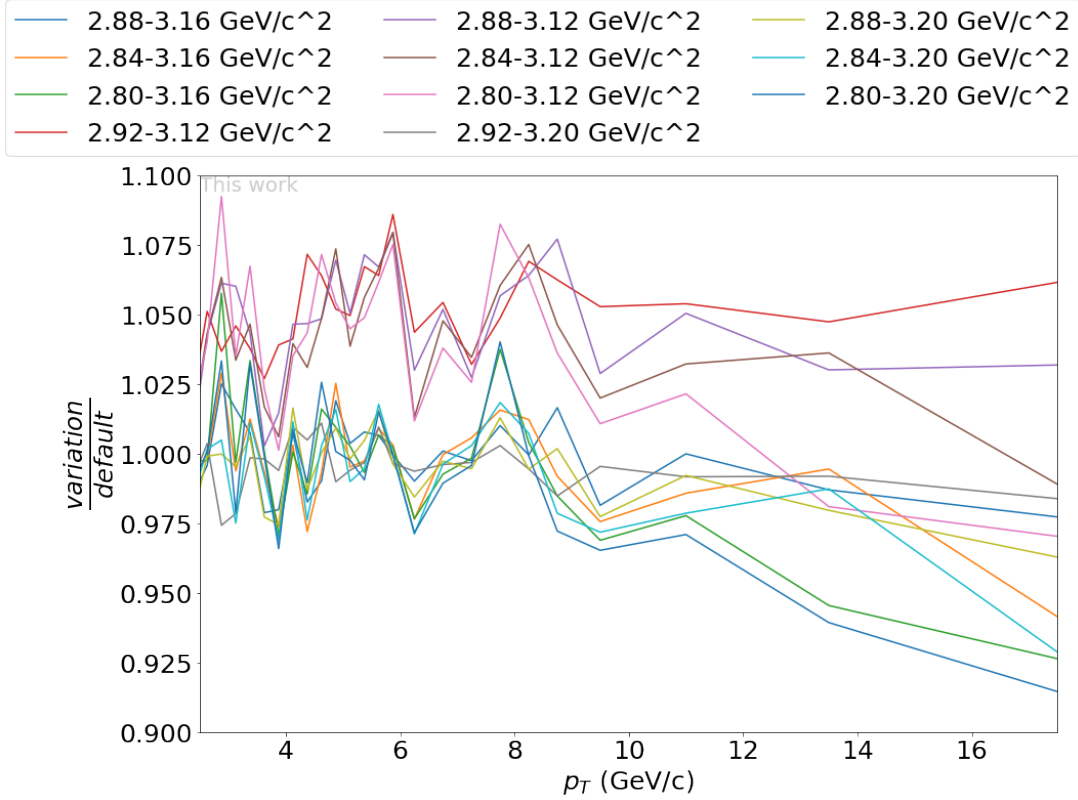
5.3.2   Mass cut range

The J/ψ signal exhibits a characteristic shape, which is sharply defined on the right side and is dominated by the bremsstrahlung tail on the left side of the peak. To determine the number of J/ψ measured during the data collection periods included, all e^-e^+ pairs falling within a specific mass range after subtracting the background are counted. With lower invariant mass, the S/B ratio gets worse which could lead to higher statistical uncertainties. Therefore, determining the influence of the mass cut range on the systematic uncertainty is crucial. These could arise from the description of the bremsstrahlung tail in MC. The default mass cut encompasses a mass region of $(2.92 - 3.16)$ GeV/c^2. The variations considered in this analysis include:

- $(2.88 - 3.16)$ GeV/c^2

- $(2.84 - 3.16)$ GeV/c^2

- $(2.80 - 3.16)$ GeV/c^2

- $(2.92 - 3.12)$ GeV/c^2

- $(2.88 - 3.12)$ GeV/c^2

- $(2.84 - 3.12)$ GeV/c^2

- $(2.80 - 3.12)$ GeV/c^2

- $(2.92 - 3.20)$ GeV/c^2

- $(2.88 - 3.20)$ GeV/c^2

- $(2.84 - 3.20)$ GeV/c^2

- $(2.80 - 3.20)$ GeV/c^2

The chosen intervals are a result of the binning that uses steps of 0.04 GeV/c^2. When plotting the ratio of variation to default as a function of p$_\text{T}$ (see Figure 5.3), it becomes evident that there is a substantial difference between the cuts with their upper limit at 3.12 GeV/c^2 and the other cuts. This observation indicates that the MC simulation of the right side of the J/ψ peak differs more from the measured data than the left side. The same result can be found in the Minimal Bias (MB) analysis of J/ψ production [2].

All methods in all p$_\text{T}$-bins successfully pass the Barlow check. Consequently, the mass cut does not introduce a systematic uncertainty and is not factored into the results.

Figure 5.3: Variation of mass cut range for individual p_T-intervals

5.3.3 Track selection criteria

As explained in Section 4.1, various criteria are employed to select good tracks. Altering these criteria can proof whether the experimental setup and the MC simulation align. The track cut variations used in this analysis, along with their Barlow check results, are listed in Table 5.1.

All variations fail the barlow test which means that their barlow-value is higher than 2σ. Hence, the uncertainties can be considered systematic uncertainties and are not only a result of statistics.

As a result, all variations are incorporated into the systematic uncertainties stemming

variable	default cut	variation	barlow check
SPD	SPD any	SPD first	fail
$N_{clusters}^{TPC}$	>70	>90	fail
χ^2_{red} in TPC	0.0	0.5	fail
$|\eta|$	-0.84<η<0.84	-0.82<η<0.82	fail
p_T [GeV/c]	1.0 <p_T	0.9<p_T; 1.05<p_T	fail
$|DCA_{xy}|$ [cm]	<1.0	<0.8	fail
$|DCA_z|$ [cm]	<3.0	<2.5	fail

Table 5.1: Track cut variations and barlow check

from the track selection variations. These variations are then plotted in histograms for different p_T intervals. Their distribution around 1 is considered a gaussian distribution which allows to use equation 5.4 in order to determine the systematic uncertainties arising from the track selection criteria.

The resulting uncertainties do not change significantly throughout the whole p_T range. Calculating the mean of these uncertainties from all p_T-bins yields a systematic uncertainty of 4.93%.

5.3.4 Particle identification

Similar to the track cuts, the particle identification cuts are also varied in the analysis process. The particle identification cuts, along with their variations and the Barlow check results, are presented in Table 5.2.

All variations result in systematic uncertainties because their barlow value is higher than 2σ and therefore fail the barlow test. Consequently, they are incorporated into the particle identification cut uncertainty. The analysis of this resulting uncertainty follows the same steps as in the previous analysis.

Taking the mean over the uncertainties in all p_T-bins that are independent of p_T leads to a systematic uncertainty of 4.59%.

variable	default cut	variation(s)	barlow check
electron identification	$\in [-3.0, 3..0]$	$\in [-2.5, 3.0]$	fail
proton and pion rejection $p_T < 5$ GeV/c	3.0	2.0	fail
proton and pion rejection $p_T > 5$ GeV/c	2.0	3.0	fail

Table 5.2: Particle identification cut variations and barlow check

5.3.5 Uncertainty related to the ITS-TPC matching efficiency

To accurately reconstruct a track, it is crucial that the various detector signals align consistently. Hence, the systematic uncertainty related to the matching efficiency between the ITS and the TPC must be accounted for as well.

The ITS-TPC matching systematic uncertainty for single tracks can be obtained from [2]. While not all data taking periods used in this analysis are covered in [2], it is worth noting that the matching efficiency exhibits no significant variation across different data taking periods. This allows us to employ a weighted average as the single-track matching efficiency uncertainty for all data taking periods. Although the provided uncertainties were originally determined for hadrons, earlier analyzes in p-Pb collisions have demonstrated their applicability to electrons as well [3].
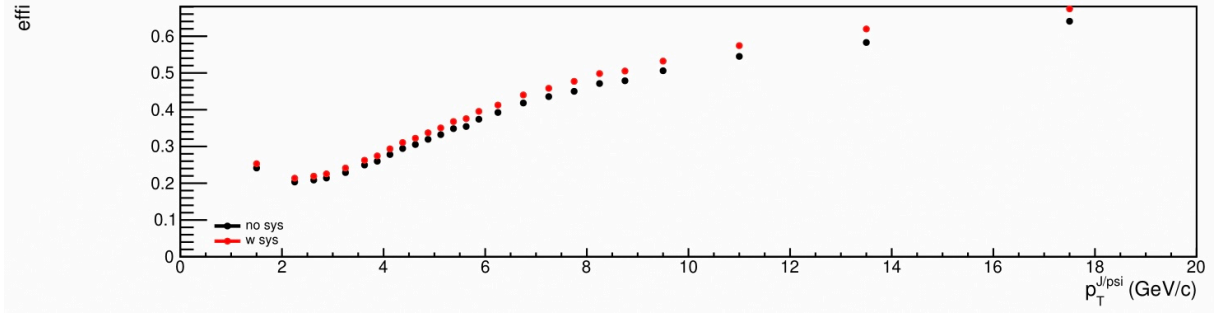
Figure 5.4: Efficiency with ITS-TPC matching uncertainty (red) and without (black)

An additional step, converting the uncertainty for a single track to an uncertainty for two tracks is necessary. To achieve this, a toy MC simulation of J/ψ mesons with a measured p_T shape and realistic decay kinematics to dielectrons is generated, incorporating a random rejection process based on the matching efficiency uncertainty of single tracks. The resulting acceptance for J/ψ is depicted in Figure 5.4, alongside the results obtained without accounting for the TPC-ITS matching uncertainties. The difference between these results is considered the systematic uncertainty attributed to the ITS-TPC matching. Since there is no dependency on p_T, the mean of the different uncertainties from all p_T-bins is used, ultimately leading to a total uncertainty of 5.16%.

5.3.6 J/ψ kinematics in MC

An accurate representation of the p_T distribution of J/ψ in the MC simulation is vital, because the acceptance and efficiency directly depend on this distribution. The systematic uncertainty stemming from the J/ψ kinematics in MC reflects how changes in the shape of the p_T distribution affect the yield of the J/ψ signal.

The p_T distribution of J/ψ in MC was already adjusted to match the previously measured data from earlier experiments. This spectrum is fitted using a power-law function:

$$A \times \left(\frac{p_T}{1 + \frac{p_T^2}{p_0^2}} \right)^n \tag{5.5}$$

with many different variations of n and p_0 within the 4σ range (see Figure 5.5(left)). These variables exhibit a strong correlation. All the slopes obtained from various fits are employed as weights to recalculate a new acceptance times efficiency. The resulting inverse efficiencies are plotted, and the root mean square (RMS) is used as the measure of uncertainty (see Figure 5.5(right)). The resulting mean uncertainty is 0.03%. This uncertainties are relatively small due to the MC J/ψ p_T shape already being generated following measurement data.
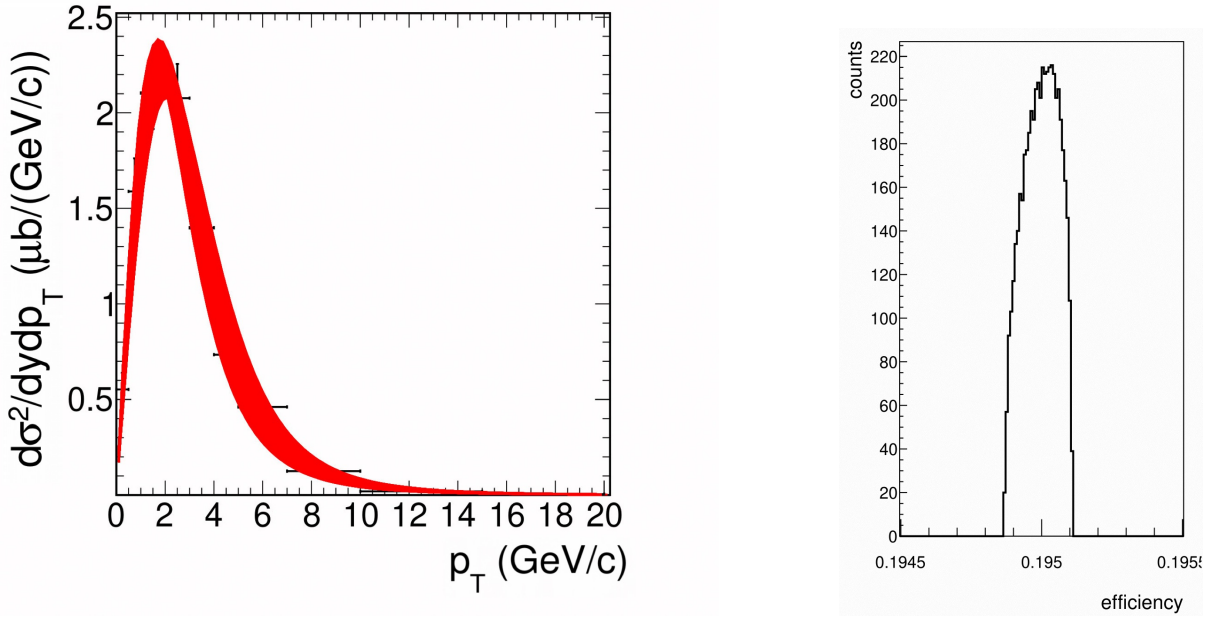
Figure 5.5: Variation of fits with different n and p_0 (left); Efficiency distribution and inverse (right)

5.3.7 Luminosity and trigger normalisation factor

Luminosity can be considered as a proportionality factor between the cross section $d\sigma/dp_T$ and the number of J/ψ per momentum interval $dN^{J/\psi}/dp_T$. This luminosity can be determined using the van der Meer cross section and the number of minimum bias (MB) events. The uncertainty associated with the van der Meer cross section is the dominant factor in this calculation.

Since this analysis focuses solely on TRD-triggered data, a trigger normalization factor of 569.679 with an error of 0.01% is used, signifying that approximately 570 MB events correspond to one TRD-triggered event [18]. The luminosity of the TRD events is calculated based on data from 2017 and 2018, resulting in a total luminosity of $(1.71 \cdot 10^9 \pm 4 \cdot 10^7)$ mb^{-1}. As a result, the relative uncertainty is found to be 2.33% due to the van der Meer systematic uncertainty.

5.3.8 Branching ratio

The branching ratio of the $J/\psi \rightarrow e^+e^-(\gamma)$ decay can be found in the PDG, see Figure 2.2. From the branching ratio

$$\Sigma/\Sigma_i = (5.971 \pm 0.032)\% \tag{5.6}$$

the relative uncertainty of 0.54% can be calculated.

Chapter 6

Results and Discussion

In Chapter 5, various sources of systematic uncertainties were analyzed and quantified. The results are summarized in Table 6.1. All uncertainties listed in this table failed the barlow-check and can therefore be considered systematic uncertainties. This table also incorporates results from the MB analysis of J/ψ production in pp collisions at $\sqrt{s} = 13$ TeV [1] to facilitate a comparison between this analysis and previous findings.

In this analyzes, the mean of the uncertainties in all p_T-bins is considered to be the systematic uncertainty over the whole p_T range if the uncertainties did not depend on p_T. The MB analysis does not take the mean but displays the uncertainties as a range from the lowest to the highest uncertainty in the p_T-region. While providing intervals of uncertainties has the advantage of quantifying fluctuations across the p_T bins more clearly, this information does not reveal whether, for instance, a significant portion of the uncertainties within the corresponding interval is closer to the lower or upper value. Furthermore, expressing uncertainties in intervals conveys a level of precision that does not inherently arise from the method used to quantify systematic uncertainties. This will be discussed in the next chapter.

Most uncertainties are slightly higher than those in the MB analysis. This trend aligns with the findings from p-Pb collisions [3].

Specifically, the background description for $p_T > 15$ GeV/c exhibits significantly high uncertainties. In the analysis presented in [1], the data in this high p_T range are obtained using the EmCal trigger, which provides higher statistics. To investigate whether these high uncertainties result from low statistics in the higher p_T range, adopting a broader p_T binning approach could potentially improve the statistics within each bin and, consequently, lead to a more precise background description. An analysis with larger bins in this range ($[12 - 20]$GeV/c and $[20 - 40]$GeV/c) yielded results that passed the Barlow test and can therefore be attributed to statistical fluctuations rather than systematic

syst. uncertainty	TRD-triggered	MB
	$2\ \text{GeV}/c < \text{p}_\text{T} < 15\ \text{GeV}/c$	$\text{p}_\text{T} < 15\ \text{GeV}/c$
Background description	3.2%	(0.2-1.2)%
Mass cut range	no systematic effect	(1.4-2.2)%
Track cuts	4.9%	3.7%
Particle identification	4.6%	(0.0-4.1)%
ITS-TPC matching	5.2%	(2.8-5.4)%
J/ψ kinematics in MC	0.03% (negligible)	(0.0-0.9)%
Luminosity	2.3%	1.6%
Branching ratio	0.5%	0.5%
Global	2.4%	1.7%
Total (w/o global)	9.1%	(5.3-7.5)%

Table 6.1: Systematic uncertainties and comparison with MB results [1]

uncertainties.

For $\text{p}_\text{T} < 2\ \text{GeV}/c$, the background description proves to be insufficient, resulting in high uncertainties. This underscores that restricting the p_T range for data analysis based on TRD-triggered events to $2\ \text{GeV}/c < \text{p}_\text{T} < 15\ \text{GeV}/c$ appears to yield the most reliable results.

The uncertainty arising from the mass cut range is not considered a systematic uncertainty in the analyzed data-taking periods because all variations pass the barlow test which means that fluctuations are statistical and should not be considered systematic. Therefore, the description of the bremsstrahlung tail in MC seems to be sufficient.

The variations in track selection criteria, which assess the quality of the MC simulation of different components of the experiment, result in systematic uncertainties that significantly contribute to the overall systematic uncertainty.

While the systematic uncertainty of the particle identification is determined through a cut variation in this analysis, the MB analysis in [1] employs a data-driven approach based on tagged photon conversions in both data and MC simulations. By comparing electron particle identification and hadron rejection in both systems, the systematic uncertainty can be quantified. This approach yields more reliable and less conservative results, serving as an example of a superior method for determining systematic uncertainties compared to cut variations.

The uncertainty related to the ITS-TPC matching efficiency is the highest among all analyzed effects. This result aligns with the MB analysis.

However, the uncertainty arising from the J/ψ kinematics in MC is very small compared to the other uncertainties and is therefore negligible. This is due to the MC J/ψ p_T shape already being generated based on measured data, which appears to be a good choice.

The global uncertainties arising from the branching ratio and the luminosity are similar to the results in the MB analysis. The branching ratio does not depend on the trigger and is therefore the same. A difference in the luminosity uncertainties from MB and TRD-triggered data could be a result from the slightly different data used ([1] uses data from 2016-2018) and a new determination of the luminosity uncertainty between the two analysis.

In general, the method of determining systematic uncertainties described in this thesis should be considered as a relatively conservative upper bound. According to Barlow, variations should not be used to quantify systematic uncertainties but rather to identify errors in the analysis process.

The results appear reasonable when compared to those from the MB analysis.

However, it is important to acknowledge potential sources of inaccuracies in uncertainty estimation. Firstly, the cut variations may seem somewhat arbitrary. To obtain highly precise results, extreme variations could be considered, such as removing all constraints on the examined cut. However, such extreme variations would introduce excessive background, preventing accurate particle reconstruction. Therefore, smaller variations are chosen, which, in turn, result in a less precise characterization of systematic uncertainties.

Another limitation of this method for determining systematic uncertainties is that it doesn't explain the underlying physical reasons for the discrepancy between the MC simulations and the actual measured data. Consequently, it becomes more challenging to identify strategies for minimizing systematic uncertainties.

Other possibilities that could be elaborated in the future to get more reliable results are described in the next chapter.

Chapter 7

Summary and outlook

7.1 Summary

This thesis investigated the systematic uncertainties in the measurement of J/ψ signals in the di-electron channel with the ALICE Detector at the LHC in 2017 and 2018 in TRD-triggered pp collisions at a center-of-mass energy of $\sqrt{s} = 13$ TeV. To evaluate systematic uncertainties originating from differences in detector acceptance and efficiency between Data and Monte Carlo (MC), variations to the background description, mass cut range, track cuts, and particle identification criteria in comparison to the default selection criteria were made. Additionally, systematic uncertainties arising from the ITS-TPC matching were quantified using single-track uncertainties and a Toy Monte Carlo approach to propagate the uncertainty to the pair level. The deviation from J/ψ kinematics in the Monte Carlo simulation was determined through variations of two parameters of a power-law function that describes the J/ψ kinematics. The resulting efficiency distribution from all variations allowed determining the resulting uncertainty. Global uncertainties such as luminosity and branching ratio were also investigated. To calculate the luminosity uncertainty, the van der Meer cross-section and the number of events were utilized. The branching ratio and its uncertainty were taken from the Particle Data Group.

Overall, this results in an uncertainty of 9.1% in the range 2 GeV/c < p_T < 15 GeV/c and above 15 GeV/c of 14.4%. The large error in these ranges is mainly dominated by the uncertainty in the background description which most likely arises from the finer binning initially selected due to the larger data sample compared to previous MB analysis. With a larger p_T binning, the background description uncertainty passes the barlow-check and can be considered a statistical fluctuation and therefore not contributing to the final systematic uncertainty. The analysis shows that measurements within a range of 2 GeV/c < p_T < 15 GeV/c yield the best results.

Overall, the results across a wide p_T range are consistent with the results from analogue measurements in MB pp collisions. However, it is important to note that these results should be considered as a conservative upper estimate of systematic uncertainties. The methodology applied, following Barlow's approach (see [6]), is more suitable as a test for identifying uncertainties in the analysis rather than quantifying systematic uncertainties.

7.2 Outlook

Although the obtained results match the results from the MB analysis, different sources of inaccuracies remain, which could be minimized in future analysis. As mentioned in Chapter 6, the arbitrary cuts don't lead to an adequate quantization of systematic uncertainties. However, the extreme variations needed for reliable results cannot be used because of the high background. Also this method doesn't provide insights into the physical source of the discrepancy between MC and data which would be necessary for further analysis.

Given that cut variations are better suited for identifying systematic uncertainties rather than quantifying systematic uncertainties, alternative methods must be explored to obtain robust results and enable the understanding of the physical origins of these uncertainties.

An effective approach involves the use of proxy samples. An example of how uncertainties arising from the ITS selection criteria can be determined from a proxy sample is provided in [26]:

To assess the detector performance for electrons, the detector performance in data and MC of unidentified charged particles can be used. This sample may include hadrons with different detector interactions than electrons. However, only the geometric distribution is used, which doesn't account for these differences in particle species. This result aligns with findings in [3]. To ensure the proxy sample's suitability, one can compare the efficiency calculated from the average of the η-normalized distribution of primary charged particles in $\eta - \phi$-space that meet the criteria with the Monte Carlo results of this distribution for electrons. Once the sample's suitability is confirmed, the systematic uncertainty arising from the ITS selection criteria can be determined by comparing the difference between measured data and simulation for the proxy sample. This method is suitable to determine systematic uncertainties arising from inaccuracies in the MC simulation's representation of detector efficiencies.

For a more detailed description of this method and alternative approaches to determine systematic uncertainties, refer to [26]. However, it's important to note that this analysis

investigates different decay processes, making it challenging to directly apply most of these methods to the analysis of $J/\psi \to e^+e^-$ or $J/\psi \to e^+e^-\gamma$ decays. However, [3] shows that there is no significant difference between electrons and hadrons in the analysis.

Another method using electrons from photon conversions identified in data and MC simulations via topological selection criteria, that is better suited for quantifying systematic uncertainties in particle identification, is briefly outlined in Chapter 6 references [1] and [3]. This approach could have been employed in this analysis to obtain a less conservative estimate of the systematic uncertainties.

In summary, identifying proxy samples that enable the comparison between data and MC simulations in specific physical properties represents a more suitable approach for determining systematic uncertainties. This method offers greater precision compared to variations, which can only provide rough and conservative upper-limit estimates.

44

Appendix A
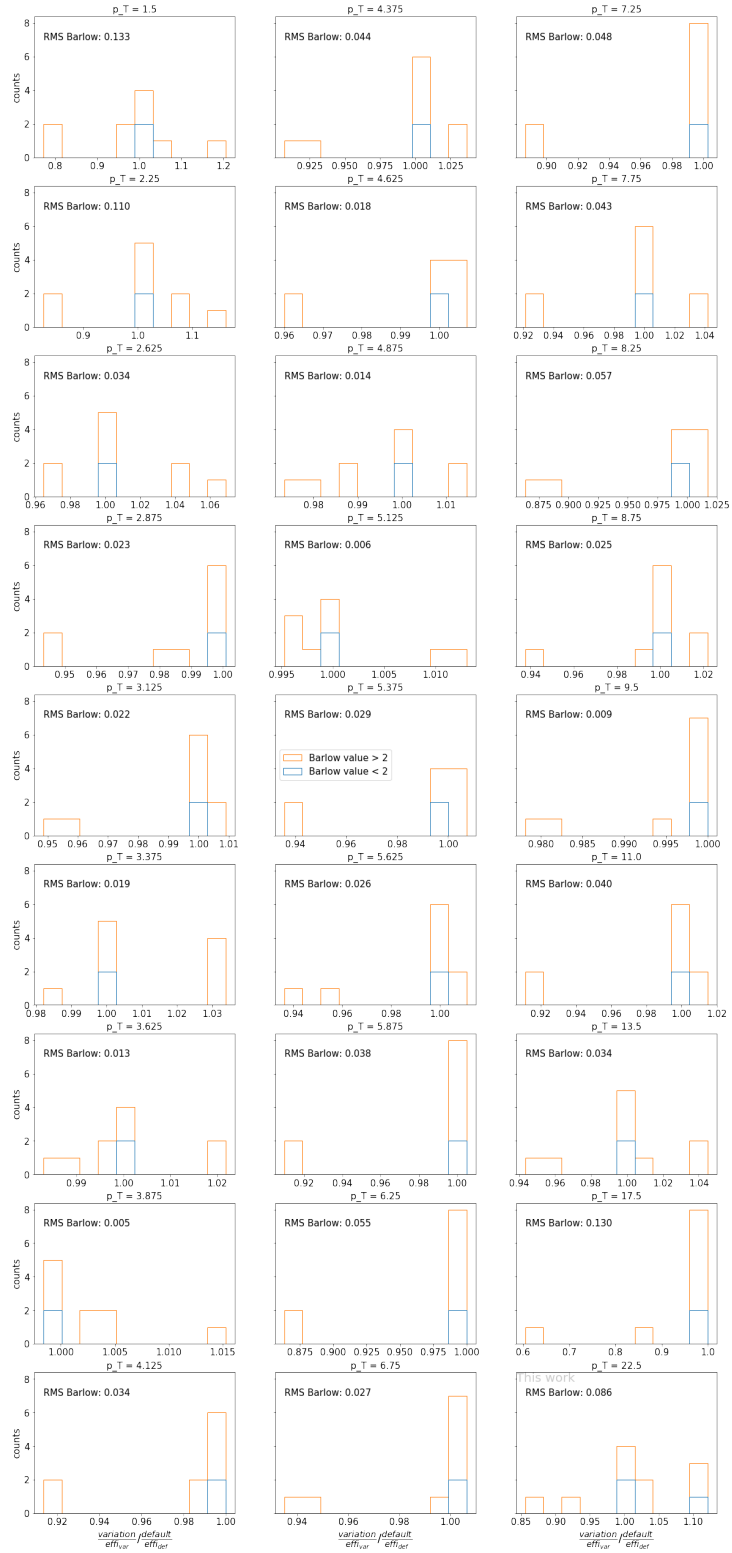
Background description histograms

Figure A.1: Variation of different background description methods for all individual p_T-intervals

Appendix B

Acknowledgements

First and foremost, I would like to express my gratitude to my advisor, Yvonne Pachmayer, whose patience and clear explanations allowed me to learn many new things. I would also like to thank Martin Völkl, who was always available whenever my knowledge of statistics reached its limit. Special thanks to Klaus Reygers for agreeing to be the second examiner.

My friends and family provided invaluable support, assisting me through meticulous proofreading and offering emotional encouragement, enabling me to believe in myself and this work.

Lastly, I would like to thank Sabine Pschorner, without whom I would not be here today. May she rest in peace.

Appendix C

Declaration

Ich versichere, dass ich diese Arbeit selbstständig verfasst und keine anderen als die angegebenen Quellen und Hilfsmittel benutzt habe.

Heidelberg, den 20.10.2023

Bibliography

[1] S. Acharya et al. (ALICE Collaboration). "Inclusive J/ψ production at midrapidity in pp collisions at $\sqrt{s} = 13$ TeV". In: *The European Physical Journal C* 81.12 (Dec. 2021). DOI: `10.1140/epjc/s10052-021-09873-4`. URL: `https://doi.org/10.1140%2Fepjc%2Fs10052-021-09873-4`.

[2] ALICE Collaboration. *Inclusive J/ψ - cross section via the di-electron channel in ALICE in MB pp collisions at $\sqrt{s} = 13$ TeV*. Analysis Note. Internal document. 2021.

[3] ALICE Collaboration. *Measurement of J/ψ in TRD-triggered p-Pb collisions at $\sqrt{s_{NN}} = 8.16$ TeV with ALICE at the LHC*. Analysis Note. Internal document. 2022.

[4] J. Alme et al. "The ALICE TPC, a large 3-dimensional tracking device with fast readout for ultra-high multiplicity events". In: *Nucl. Instrum. Meth. A* 622 (2010), pp. 316–367. DOI: `10.1016/j.nima.2010.04.042`. arXiv: `1001.1950 [physics.ins-det]`.

[5] Roger Barlow. *Systematic errors in particle physics - PWA9/athos4 - indico*. Mar. 2017. URL: `https://indico.cern.ch/event/591374/contributions/2511753/attachments/1429002/2193943/01_PWA-Barlow.pdf`.

[6] Roger Barlow. "Systematic errors: Facts and fictions". In: *Conference on Advanced Statistical Techniques in Particle Physics*. July 2002, pp. 134–144. arXiv: `hep-ex/0207026`.

[7] A. Bazavov et al. "Chiral crossover in QCD at zero and non-zero chemical potentials". In: *Phys. Lett. B* 795 (2019), pp. 15–21. DOI: `10.1016/j.physletb.2019.05.013`. arXiv: `1812.08235 [hep-lat]`.

[8] Peter Braun-Munzinger and Johanna Stachel. "The quest for the quark–gluon plasma". In: *Nature* 448.7151 (July 2007), pp. 302–309. ISSN: 1476-4687. DOI: `10.1038/nature06080`. URL: `https://doi.org/10.1038/nature06080`.

[9] ALICE Collaboration. "ALICE 2016-2017-2018 luminosity determination for pp collisions at $\sqrt{s} = 13$ TeV". In: *public note* (2021).

[10] ALICE Collaboration. "First results of the ALICE detector performance at 13 TeV". In: *public note* (2015). URL: `https://cds.cern.ch/record/2047855`.

[11] ALICE Collaboration. *The ALICE experiment – A journey through QCD*. 2022. arXiv: 2211.04384 [nucl-ex].

[12] ALICE Collaboration. "The ALICE experiment at the CERN LHC". In: *JINST* 3 (2008), S08002. DOI: 10.1088/1748-0221/3/08/S08002.

[13] ALICE Collaboration. "The ALICE Transition Radiation Detector: construction, operation, and performance". In: *Nucl. Instrum. Meth. A* 881 (2018), pp. 88–127. DOI: 10.1016/j.nima.2017.09.028. arXiv: 1709.02743 [physics.ins-det].

[14] V L Ginzburg. "Transition Radiation and Transition Scattering". In: *Physica Scripta* 1982.T2A (Jan. 1982), p. 182. DOI: 10.1088/0031-8949/1982/T2A/024. URL: https://dx.doi.org/10.1088/0031-8949/1982/T2A/024.

[15] Particle Data Group. "Review of Particle Physics". In: *PTEP* 2022 (2022), p. 083C01. DOI: 10.1093/ptep/ptac097.

[16] I Hřivnáčová et al. "The ALICE Geant4 Simulation". In: *Journal of Physics: Conference Series* 331.3 (Dec. 2011), p. 032016. DOI: 10.1088/1742-6596/331/3/032016. URL: https://dx.doi.org/10.1088/1742-6596/331/3/032016.

[17] Avinash Khare. *The November J/Ψ Revolution: Twenty-Five Years Later*. 1999. arXiv: hep-ph/9910468 [hep-ph].

[18] Yvonne Pachmayer. *Private Communication*. 2023.

[19] Andrew Purcell. "Go on a particle quest at the first CERN webfest. Le premier webfest du CERN se lance à la conquête des particules". In: 35/2012 (2012), p. 10. URL: https://cds.cern.ch/record/1473657.

[20] Michael Riordan. "The Hunting of the Quark". In: *Bulletin of Science, Technology & Society* 8.4 (1988), pp. 276–289. DOI: 10.1177/0270467688008004120. eprint: https://doi.org/10.1177/0270467688008004120. URL: https://doi.org/10.1177/0270467688008004120.

[21] Wouter Schmitz. "The Strong Force: Quantum Chromodynamics". In: *Particles, Fields and Forces: A Conceptual Guide to Quantum Field Theory and the Standard Model*. Cham: Springer International Publishing, 2022, pp. 287–320. ISBN: 978-3-030-98753-4. DOI: 10.1007/978-3-030-98753-4_18. URL: https://doi.org/10.1007/978-3-030-98753-4_18.

[22] Torbjörn Sjöstrand. "The Pythia event generator: Past, present and future". In: *Computer Physics Communications* 246 (Jan. 2020), p. 106910. DOI: 10.1016/j.cpc.2019.106910. URL: https://doi.org/10.1016%2Fj.cpc.2019.106910.

[23] Davison E. Soper. *Basics of QCD Perturbation Theory*. 1997. arXiv: hep-ph/9702203 [hep-ph].

[24] Mark Thomson. *Modern Particle Physics*. Cambridge University Press, 2013. DOI: 10.1017/CBO9781139525367.

[25] Samuel C. C. Ting. "The Discovery of the J Particle". In: *NATO Sci. Ser. B* 352 (1996). Ed. by Harvey B. Newman and Thomas Ypsilantis, pp. 303–327. DOI: 10.1007/978-1-4613-1147-8_16.

[26] Martin Völkl. "Electrons from Beauty-Hadron Decays in Central Pb-Pb Collisions at $\sqrt{s_\mathrm{NN}} = 2.76$ TeV". PhD thesis. Heidelberg, Germany: Ruperto-Carola-University of Heidelberg, 2016.

[27] Felix Korbidian Waldherr. "ALICE TRD electron trigger performance in pp collisions at $\sqrt{s} = 13$ TeV". Bachelor's Thesis. Ruperto-Carola-University of Heidelberg, 2022.

[28] Z. Was, P. Golonka, and G. Nanava. *PHOTOS Monte Carlo for precision simulation of QED in decays - History and properties of the project.* 2007. arXiv: 0707.3044 [hep-ph].

[29] K. Yagi, T. Hatsuda, and Y. Miake. *Quark-Gluon Plasma: From Big Bang to Little Bang.* Cambridge Monographs on Particle Physics, Nuclear Physics and Cosmology. Cambridge University Press, 2005. ISBN: 9780521561082. URL: https://books.google.de/books?id=C2bpxwUXJngC.